



Ionospheric irregularity reconstruction using multisource data fusion via deep learning

Penghao Tian¹, Bingkun Yu^{2,1,3}, Hailun Ye¹, Xianghui Xue^{1,3,4}, Jianfei Wu¹, and Tingdi Chen^{1,3}

¹Deep Space Exploration Laboratory/School of Earth and Space Sciences,
University of Science and Technology of China, Hefei, China

²Institute of Deep Space Sciences, Deep Space Exploration Laboratory, Hefei, China

³Anhui Mengcheng Geophysics National Observation and Research Station,
University of Science and Technology of China, Hefei, China

⁴Hefei National Laboratory, University of Science and Technology of China, Hefei, China

Correspondence: Bingkun Yu (bkyu@ustc.edu.cn) and Xianghui Xue (xuexh@ustc.edu.cn)

Received: 14 June 2023 – Discussion started: 19 June 2023

Revised: 20 August 2023 – Accepted: 25 August 2023 – Published: 24 October 2023

Abstract. Ionospheric sporadic E layers (Es) are intense plasma irregularities between 80 and 130 km in altitude and are generally unpredictable. Reconstructing the morphology of sporadic E layers is not only essential for understanding the nature of ionospheric irregularities and many other atmospheric coupling systems, but is also useful for solving a broad range of demands for reliable radio communication of many sectors reliant on ionosphere-dependent decision-making. Despite the efforts of many empirical and theoretical models, a predictive algorithm with both high accuracy and high efficiency is still lacking. Here we introduce a new approach for Sporadic E Layer Forecast using Artificial Neural Networks (SELF-ANN). The prediction engine is trained by fusing observational data from multiple sources, including a high-resolution ERA5 reanalysis dataset, Constellation Observing System for Meteorology, Ionosphere, and Climate (COSMIC) radio occultation (RO) measurements, and integrated data from OMNIWeb. The results show that the model can effectively reconstruct the morphology of the ionospheric E layer with intraseasonal variability by learning complex patterns. The model obtains good performance and generalization capability by applying multiple evaluation criteria. The random forest algorithm used for preliminary processing shows that local time, altitude, longitude, and latitude are significantly essential for forecasting the E-layer region. Extensive evaluations based on ground-based observations demonstrate the superior utility of the model in dealing with unknown information. The presented framework will help us better understand the nature of the ionospheric irregularities, which is a fundamental challenge in upper-atmospheric and ionospheric physics. Moreover, the proposed SELF-ANN can make a significant contribution to the development of the prediction of ionospheric irregularities in the E layer, particularly when the formation mechanisms and evolution processes of the Es layer are not well understood.

1 Introduction

Ionospheric E-layer irregularities, or sporadic E (Es), are dense layers of metallic ions in the lower thermosphere between 80 and 130 km, a region that is characterized by complicated atmospheric dynamics and nonlinear plasma processes (Matsushita and Reddy, 1967; Whitehead, 1970; Mathews, 1998; Haldoupis, 2011). The intense plasma ir-

regularities within Es layers, which are representative of the complex interaction between the neutral atmosphere and the ionosphere, can cause perturbations and scintillation in radio signals due to a large vertical gradient in electron density (Pavelyev et al., 2007; Zeng and Sokolovskiy, 2010; Sokolovskiy et al., 2014). The phenomenon has attracted considerable attention over the last decades, which led to numerous scientific studies (Arras et al., 2008; Lei et al.,

2007, 2008; Chu et al., 2014; Tsai et al., 2018; Arras and Wickert, 2018; Yu et al., 2019; Shinagawa et al., 2021; Ye et al., 2023). However, the reconstruction of the global ionospheric Es layer is a particular challenge due to the different mechanisms responsible for the formation and spatiotemporal variations of Es layers at different latitudes (Carter and Forbes, 1999; Whitehead, 1961, 1989; Raghavarao et al., 2002; Kirkwood and Nilsson, 2000; Lühr et al., 2021; MacDougall et al., 2000). Generally, the Es layer occurs at all latitudes and longitudes around the globe, but it has traditionally been divided into three classes: equatorial or low-latitude, temperate or mid-latitude, and aurora or high-latitude, each assumed to represent rather different formation mechanisms (Kirkwood and Nilsson, 2000). The most favored explanation for the formation of mid-latitude Es layers is the wind-shear mechanism (Whitehead, 1961, 1989). According to this theory, long-lived metallic ions are gathered into thin layers due to vertical shears in the horizontal winds. Equatorial or low-latitude Es layers appear to be two types, one of which is the same as mid-latitude Es, and another is caused by plasma instabilities associated with the equatorial electrojet (Raghavarao et al., 2002). High-latitude or auroral Es were long assumed to be a manifestation of the aurora, in which keV electrons precipitate into the upper atmosphere, exciting oxygen and nitrogen and resulting in both auroral emission and a strong, sporadic source of enhanced E-region ionization (Kirkwood and Nilsson, 2000). Therefore, the modeling of ionospheric E-layer morphology and dynamics is essential for the near-real-time forecast and long-term prediction of the ionospheric parameters to serve satellite-based communication and navigation needs (Li et al., 2021).

Since the first theoretical descriptions of the ionospheric layers by Chapman (1931a, b), empirical or theoretical models have been developed by understanding the physical, chemical, and transport processes that control the variability of coupled thermosphere–ionosphere systems. For instance, the International Reference Ionosphere (IRI), Thermosphere-Ionosphere-Electrodynamics General Circulation Model (TIE-GCM), Thermosphere-Ionosphere-Mesosphere-Electrodynamics General Circulation Model (TIME-GCM), and Ground to topside model of the Atmosphere and Ionosphere for Aeronomy (GAIA) are some of the well-established empirical or theoretical models that are widely used in ionospheric modeling (Bilitza et al., 2022; Priyadarshi, 2015; Qian et al., 2014; Roble and Ridley, 1994; Jin et al., 2011). Apart from the ionospheric numerical models mentioned above, several studies have proposed empirical and theoretical models specifically tailored to the E layer that assist in gaining a deeper insight into the evolution of the E-region morphology. Titheridge (2000) provided a refined set of equations for modeling the peak of the ionosphere E layer, building upon the IRI model and giving a good overall representation of the E regions of the ionosphere. Resende et al. (2017) employed the Ionospheric E-Region Model (MIRE) to investigate the competition between tidal winds and elec-

tric fields in the formation of blanketing Es layers. Yu et al. (2022) constructed an empirical model of the Es layers using the multivariable nonlinear least-squares-fitting method, which provides a comprehensive description of the climatology and global variation of Es layers.

The earlier studies have, to a certain extent, contributed to our comprehension of the complicated interaction between various factors that influence the formation and variability of the Es layer. However, discrepancies arise between the results of conventional models and real-world observations regarding the reproduction of Es local morphology, especially when analyzing the short-term evolution. The primary reason is the complex formation mechanism of the Es layer, which involves various physical phenomena such as gravity wave breaking in the upper atmosphere (Djuth et al., 2010; Vadas and Liu, 2009), the combined effects of ionospheric electric fields and horizontal neutral winds (Nygren et al., 1984; Shinagawa et al., 2017; Yu et al., 2021b), intense geomagnetic activities (Thayer and Semeter, 2004; Johnson and Heelis, 2005; Pedatella, 2016), and chemical reactions of metallic ions (Plane, 2012; Wu et al., 2021). This complexity poses a significant challenge to traditional methods to capture all the underlying physical mechanics accurately. For instance, Shinagawa et al. (2021) conducted a comparison between the vertical ion convergence (VIC) by wind shear obtained from the GAIA model and the observed critical frequency of the Es layer (f_oEs) from an ionosonde. The correlation coefficients at 110 and 130 km altitude are only 0.35 and 0.34, respectively. It is still difficult to numerically reproduce the Es structures. Furthermore, with the continued increase in missions devoted to exploring the vicinity of Earth's space, an extensive array of data has been amassed. Notable examples of these include the Global Positioning System/Meteorology (GPS/MET), Challenging Mini-satellite Payload (CHAMP), Gravity Recovery and Climate Experiment (GRACE), and FORMOSA SATellite-3/Constellation Observing System for Meteorology, Ionosphere, and Climate (FORMOSAT-3/COSMIC), among others. Regrettably, traditional models have proven inadequate for fully harnessing this vast volume of data.

Reincarnation of artificial neural networks (ANNs) in the form of deep learning has improved the accuracy of several pattern recognition tasks, such as classification of objects, scenes, and various other entities in digital images (Schmidhuber, 2015; LeCun et al., 2015; Silver et al., 2017). The rapid and pervasive progress of artificial intelligence (AI) research has profoundly influenced several scientific domains, including geoscience (Reichstein et al., 2019; Ham et al., 2019; Salcedo-Sanz et al., 2020; Yu and Ma, 2021). Examples include conditional generative adversarial networks to generate far-side solar magnetograms (Kim and Cho, 2019) and random forest algorithms for assessing skill in forecasting marine heatwaves (Giamalaki et al., 2022) and to study the presence of post-storm cooling in the middle thermosphere using artificial neural networks (Licata et al., 2022), to

name a few. It has been demonstrated that machine learning confers significant advantages in the field of fitting complex coupled systems as opposed to conventional methodologies that typically rely on experimental or physical models.

Notably, while deep learning has gained increasing traction in the geosciences field, there remains a lack of research applying artificial intelligence techniques for the prediction of global Es-layer morphology. Tian et al. (2022) apply the deep-learning approach, which is adapted from 3D U-Net, to extract the latent correlation between the lower atmosphere and the global ionospheric Es layer. Comprehensive quantitative analysis is also provided through multiple evaluation metrics. The work has made a significant contribution to global Es-layer modeling using machine-learning techniques. However, limitations persist in the study, particularly in terms of interpretability and serviceability.

Hence, we present a new deep-learning model for Sporadic E Layer Forecast using Artificial Neural Networks, called SELF-ANN, to reconstruct the structure of the global Es layer by employing multisource data fusion, as illustrated in Fig. 1. The proposed algorithm is implemented by fusing observational data from multiple sources, including the high-resolution European Centre for Medium-Range Weather Forecasts (ECMWF) reanalysis v5 (ERA5) dataset, FORMOSAT-3/COSMIC radio occultation (RO) measurements, and integrated data from OMNI. To assess the relative importance of individual variables, such as the troposphere, stratosphere, and geomagnetic and solar activities, in the prediction of the model, we employed a conventional machine-learning method, i.e., random forest regression (RFR). The results indicate that the local spatiotemporal information of the E region exhibits a more significant association with Es occurrence than other types of features. In addition, comprehensive statistical analysis reveals a correlation coefficient of 0.607 between the prediction of the model and the observation from the COSMIC RO dataset. This trained model is particularly effective at forecasting the morphology distribution and seasonal evolution of the Es layer, whose formation mechanism and underlying processes are complex. Additional validation was conducted using the *foEs* data obtained from an ionosonde station situated in Beijing, China, to ensure the generalizability of the SELF-ANN model. The hourly correlation coefficient between the observed *foEs* data and the model prediction reaches 0.531, thereby providing confidence in the practical utility of the model. We have designed and implemented a graphical user interface (GUI) that integrates a well-trained model and presents a user-friendly interface. The open-source software tool is freely available for the specific needs of researchers in the community who are interested in the Es layer. Moreover, this tool can facilitate the exploration of large-scale variations of the Es layer and other climate features as well as the incorporation of ionosonde observations via data assimilation, resulting in a better description of the sporadic E-layer distribution.

2 Methods

2.1 Data

ERA5, the latest iteration of reanalysis data provided by the ECMWF, represents a significant advancement over its predecessor, ERA-Interim. Released in 2016, ERA5 offers enhanced resolution capabilities with a comprehensive coverage of 137 hybrid sigma–pressure (model) levels along the vertical axis, spanning 1012 hPa (0.01 km) to 0.01 hPa (80.3 km) (Hersbach et al., 2020). Notably, ERA5 incorporates a multitude of reprocessed datasets and incorporates recent instrumentation that was not integrated into ERA-Interim, supplementing traditional observation data sourced from the Global Telecommunication System. A key addition to ERA5 is the inclusion of data from the Aeolus satellite, the first global wind measurement satellite launched by the European Space Agency (ESA). This new dataset provides invaluable wind measurements, augmenting ERA5's accuracy and reliability. In this study, the reanalysis production provides the high-resolution data for the lower atmosphere, which are utilized as the input information.

The FORMOSAT-3/COSMIC constellation is comprised of six microsatellites that traverse the Earth's orbit at an initial altitude of 800 km (Rocken et al., 2000; Schreiner et al., 2007; Anthes et al., 2008). These microsatellites are tasked with performing radio occultation measurements, which allows for the collection of data on both the neutral atmosphere and the ionosphere. Ionospheric scintillation of radio signals occurs when a radio wave passes through plasma density irregularities in the ionosphere (Weber et al., 1985). The S4 index is defined as the standard deviation of the detrended intensity of received signals normalized to the average signal intensity (Briggs and Parkin, 1963; Yue et al., 2014; Schreiner et al., 2011). This index has proven to be an effective measure for quantifying ionospheric scintillation, and it is widely used in research (Yue et al., 2014; Yu et al., 2019, 2020, 2021a; Arras et al., 2009; Arras and Wickert, 2018; Ye et al., 2021, 2023). Moreover, the OMNI dataset, a multisource data collection of the near-Earth solar wind environment with hourly resolution, serves as auxiliary data for this research; i.e., it provides geomagnetic and solar activity information (King and Papitashvili, 2005; Papitashvili and King, 2020).

The objective of our research is to establish latent mapping connections between external driving factors and the ionospheric E region. The present study has opted for lower-atmospheric parameters (e.g., wind, temperature) and measures of geomagnetic and solar activities as the raw input variables. The ionospheric irregularities in the E region were represented by the maximum values of amplitude scintillation S4 index (S4max) data observed at altitudes between 80 and 130 km during a 7-year period spanning 2008 to 2014. We employed linear interpolation to obtain the raw input variables based on spatiotemporal information from each

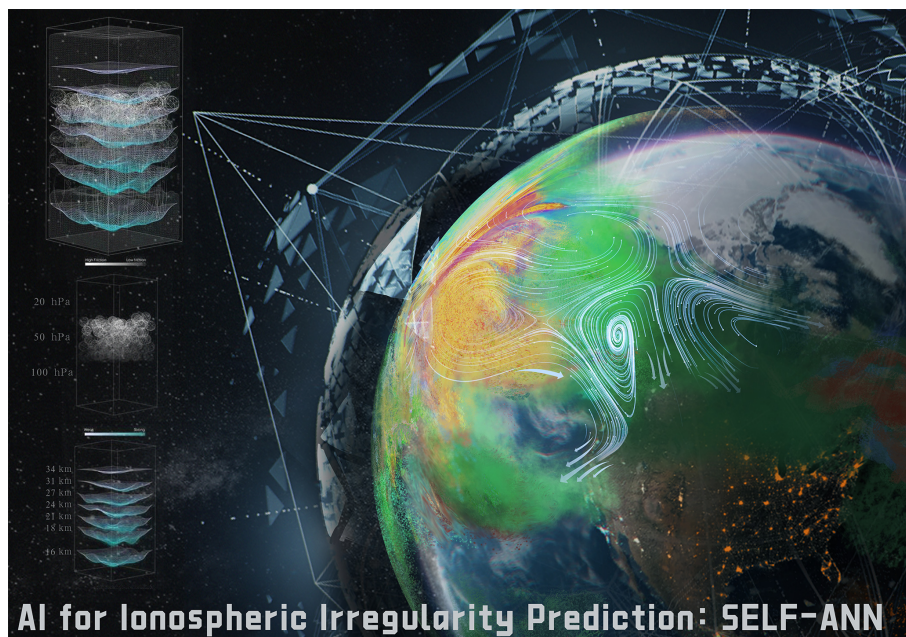


Figure 1. An illustrative diagram of the intricate integration of artificial intelligence techniques with multisource data for the prediction of upper-atmospheric and ionospheric evolution.

valid RO sample. A uniform sampling strategy was utilized to divide the entire dataset with the aim of ensuring the inclusion of ionospheric information from different solar activities in the training procedure. In summary, the collected RO measurements were partitioned into three sets for the purposes of training, validation, and testing; i.e., the sampled data, about 20 %, were designated as the test set (937 592 samples), while the remaining data were utilized as the training (3 562 999 samples) and validation (187 527 samples) sets. Since the S4max index correlates well with f_oE_s measured from the global ground-based ionosonde (Lei et al., 2007; Yu et al., 2019, 2020), we selected ionosonde data from Beijing, China, to validate the generalizability of the model. More detailed information about the raw input variables and preprocessing is given in Sect. S1.3 and Table S1 in the Supplement.

2.2 Algorithms

The random forest (RF) algorithm is a nonparametric statistical learning method that uses an ensemble of decision trees and can be applied to both regression and classification problems (Breiman, 2001; Svetnik et al., 2003). The RF is performed based on the principles underlying the classification and regression tree (CART) model strategy (Breiman, 2017). To construct an individual decision tree, smaller subgroups of observations of the predictors, also known as features, are created using optimal decision rules, or split rules. This balances the prevalent overfitting problem, minimizes variance, and ensures improved accuracy by creating several trees for different subsets of the data points. These groups are split in a

way that maximizes the difference in predicted variables between the groups while also maximizing their homogeneity within the groups. Creating several trees for different subsets of the data points balances the prevalent overfitting problem, minimizes variance, and ensures improved accuracy. In regression problems, the predicted value of the RF is determined by the average aggregation of all the decision trees.

The RF ranks the input variables by a variable importance measure, which reflects the impact of the input variables on the output based on the prediction accuracy (Breiman, 2017). We utilized this approach to perform a preliminary importance analysis of all the input variables, facilitating the subsequent selection of effective input information for training. The samples for constructing the RF model were obtained through a process of downsampling from the original training set. The predictive performance of the RF model is improved by increasing the tree strength and decreasing the number of correlations among trees. Empirical studies have previously shown that the maximum RF model performance is often achieved by the first 100 trees; i.e., a larger number of trees in a forest can not necessarily improve performance (Oshiro et al., 2012; Couronné et al., 2018). Therefore, a base model of 100 trees was selected for the regression task. A sample size of at least two data points to split an internal node and at least one point is needed for a terminal node.

In recent years, deep neural networks have seen preliminary success in climate science, meteorology, and hydrology, resulting in improved predictive skills and the development of methods to investigate the spatiotemporal dependencies (Ham et al., 2019; Liu et al., 2023). Sufficient evidence re-

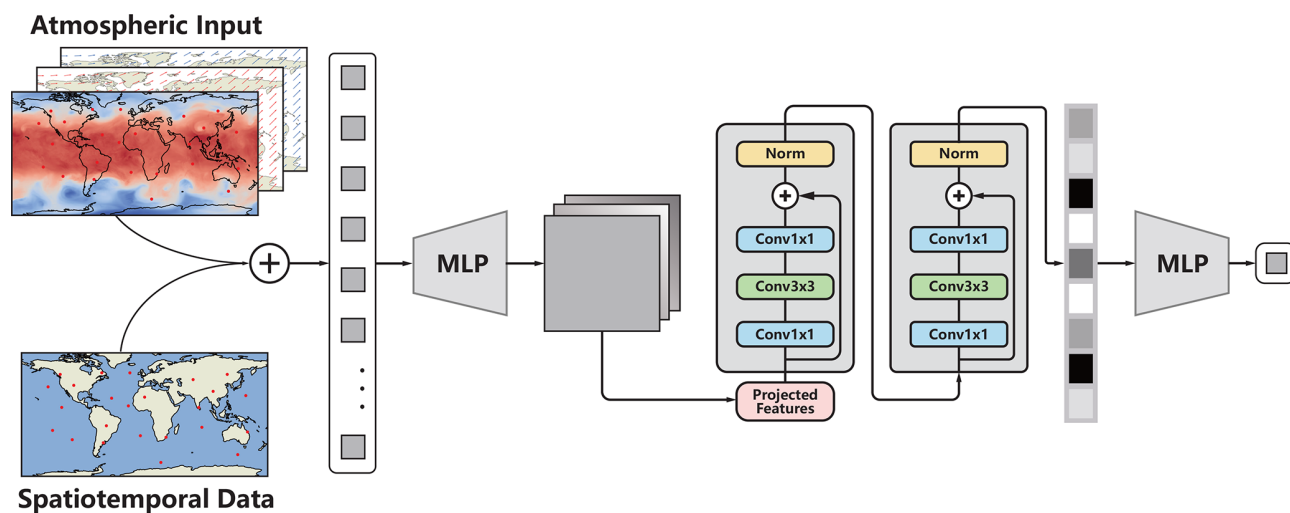


Figure 2. Overall framework of SELF-ANN (Sporadic E Layer Forecast using Artificial Neural Networks). MLP represents several dense layers composed of multilayer perceptrons. The conv 1×1 and conv 3×3 denote convolution layers with convolutional kernels of 1 and 3, respectively. “Norm” refers to batch normalization operation. The number of neurons depicted is not representative.

veals that network depth is of crucial importance (Simonyan and Zisserman, 2014; Szegedy et al., 2015). Excessive depth in neural networks can lead to the notorious problem of vanishing or exploding gradients (Bengio et al., 1994; Glorot and Bengio, 2010). This issue arises when the gradients of the loss function with respect to the model parameters become too small or too large during backpropagation. As a result, the learning process can slow down significantly or even fail to converge. The Residual network (ResNet) (He et al., 2016) is a type of neural network that alleviates this problem of training deep-learning networks by using skip connections in every stacked block, which provides alternative paths for original and derived features, rendering training faster and more efficient. We proposed the SELF-ANN model, which has incorporated dense blocks at the front and back ends to adapt to input data based on the residual network architecture, as shown in Fig. 2. The detailed structure of the SELF-ANN module can be found in Table S2.

The lower-atmospheric data and spatiotemporal information are first subjected to feature fusion, followed by standardization, a regular preprocessing operation, before being fed into the model. Figure 2 illustrates the SELF-ANN architecture, which consists of the convolutional layer (conv 1×1 or conv 3×3), batch normalization (norm) units (Ioffe and Szegedy, 2015), residual blocks (ResBlock), and a full connection layer composed of multilayer perceptrons (MLPs). Each ResBlock consists of three convolution layers, followed by a rectified linear activation unit (ReLU) activation function (Nair and Hinton, 2010) and batch normalization, where it protects the integrity of geoscience information through skip connections. Such skip connections, or shortcuts, are those that skip one or more layers and simply perform identity mapping as expressed by the following equation:

$$y = \mathcal{F}(x, W_i) + W_s x. \quad (1)$$

Here, x and y are input and output vectors of the layers considered. The function $\mathcal{F}(x, \{W_i\})$ represents the learned abstract mapping. W_s is a linear projection to match the dimensions of x and \mathcal{F} . The aggregate features via shortcuts will perform batch normalization, which is an important way of addressing the problem of vanishing or exploding gradients. In the context of batch normalization, the calculation of the mean and variance of a batch of images can be expressed using Eqs. (2) and (3), respectively. The resulting values are subsequently utilized in Eq. (4) to perform normalization, followed by Eq. (5) for scaling and shifting. The detailed formulas are listed as follows:

$$\mu_n = \frac{1}{n} \sum_{i=1}^n x_i, \quad (2)$$

$$\sigma_n^2 = \frac{1}{n} \sum_{i=1}^n (x_i - \mu_n)^2, \quad (3)$$

$$\hat{x}_i = \frac{x_i - \mu_n}{\sqrt{\sigma_n^2 + \varepsilon}}, \quad (4)$$

$$\hat{y}_i = \gamma \hat{x}_i + \beta, \quad (5)$$

where n represents the batch size, x_i refers to the i th value of x , μ_n and σ_n^2 denote the mean and variance of x , \hat{x}_i means the output of batch normalization, ε represents an infinitely small value, γ and β represent the parameters of scaling, and \hat{y}_i is the final scaled output. The ReLU activation function is used after batch normalization. As expressed in Eq. (6), the operation outputs 0 when $\hat{y}_i \leq 0$ and conversely outputs

a linear mapping when $\hat{y}_i > 0$.

$$\text{ReLU}(\hat{y}_i) = \begin{cases} l\hat{y}_i & \text{if } \hat{y}_i > 0 \\ 0 & \text{if } \hat{y}_i \leq 0 \end{cases} \quad (6)$$

The SELF-ANN source code was implemented in Python with the PyTorch package and trained on a remote-server node with eight 80 GB NVIDIA A100-SXM4 graphics processing units (GPUs), dual 32-core Intel® Xeon® Platinum 8358 CPUs at 2.6 GHz, and 1 TB of RAM. The mean absolute error loss function is used during the training process. Batch normalization is implemented to accelerate training by reducing internal covariate shift (Ioffe and Szegedy, 2015). The Nadam optimizer is employed to optimize the predefined loss function where the approach is robust in deep learning (Ruder, 2016). The learning rate is initially set to 0.0002, a critical parameter in this research, and the batch size is set to 256. In addition, we used a technique for tweaking the learning rate scheduler, called ReduceLROnPlateau, to vary the learning rate depending on the number of epochs to accelerate the model's convergence (Bowling and Veloso, 2002). The technique monitors a quantity and reduces the learning rate when that quantity stops improving.

2.3 Evaluation metrics

The present study employs multiple evaluation metrics to assess the performance of SELF-ANN. These metrics are calculated by quantifying the discrepancies between the observations and the model output. The following metrics are utilized:

$$\begin{cases} \text{SCC} = \frac{\text{cov}(R(\hat{y}_i), R(y_i))}{\sigma_{R(\hat{y}_i)} \cdot \sigma_{R(y_i)}}, \\ \text{ME} = \frac{1}{N} \sum_{i=1}^N (\hat{y}_i - y_i), \\ \text{MAE} = \frac{1}{N} \sum_{i=1}^N |\hat{y}_i - y_i|, \\ \text{RMSE} = \sqrt{\frac{1}{N} \sum_{i=1}^N (\hat{y}_i - y_i)^2}, \end{cases} \quad (7)$$

where SCC is the Spearman correlation coefficient, ME is the mean error, MAE is the mean absolute error, and RMSE is the root mean square error. N is the number of RO samples in the test data. y_i and \hat{y}_i are the target values, i.e., the S4max index, of the observations and predictions, respectively. $R(y_i)$ and $R(\hat{y}_i)$ are the rank values of those two variables. $\text{cov}(\cdot)$ means the covariance operation. $\sigma_{R(y_i)}$ and $\sigma_{R(\hat{y}_i)}$ are the standard deviations of $R(y_i)$ and $R(\hat{y}_i)$, respectively. Moreover, the Altman–Bland method was employed to evaluate the discrepancies between the measurements and the predictions (Altman and Bland, 1983). The method was also used to calculate the 95 % confidence limits of agreements for the estimation (average difference ± 1.96 standard deviation of the difference). Detailed calculation steps of the Altman–Bland method can be found in Sect. S1.2 in the Supplement.

3 Results

3.1 The importance of input variables

The random forest regression algorithm was utilized to evaluate the input variables, with their importance rankings established through an analysis of their impurity (Breiman, 2001; Svetnik et al., 2003). During a downsampling operation for all the data, we take the 1 562 941 vectors as input x , where each vector comprises n parameters of the lower-atmospheric information and external forcing (solar and geomagnetic), and the corresponding ionospheric scintillation index serves as output y . As it is currently unfeasible to determine the neutral wind fields in the E region, we have instead considered the lower-atmospheric variables as potential seed sources that may influence the wind fields in the ionospheric region (Kazimirovsky et al., 2003; Yiğit et al., 2016). The lower-atmospheric parameters, including variables such as wind, temperature, and geopotential, were collected from the ERA5 reanalysis dataset. Together with the spatiotemporal information of the source region of samples and external forcing such as geomagnetic and solar activities, the dimension of the x space is 52 ($n = 52$). All of the aforementioned features may play a vital role in predicting the ionospheric irregularities; however, explicitly removing irrelevant features improves both dimensionality reduction and noise elimination. The procedure for training random forest models and all input variables used for importance ranking can be found in Sect. S1.1 and Table S1, respectively, in the Supplement.

Figure 3 illustrates the importance ranking results of different input variables. The high mean decrease impurity (MDI) values obtained from the spatiotemporal location information of ionospheric irregularities, as depicted by local time, altitude, latitude, and longitude in the figure, are not unexpected, given a strong correlation with the intensity of the Es. These findings are consistent with previous research on the morphology of the Es, such as the diurnal variation of the scintillation occurrence (Ogawa et al., 1989; Yu et al., 2021b) and the global scale distribution of Es intensity (Yu et al., 2019). The zonal wind in the stratosphere ranks fifth in importance for the investigated parameters following the spatiotemporal information. It could act as a seed source affecting dynamical processes in the E region (Goncharenko et al., 2010). Additionally, geopotential and temperature variables also exhibit a significant contribution, which is an interesting result. This phenomenon can be attributed to the impact of upward propagation of internal atmospheric waves (planetary waves, tides, and gravity waves), which act as an essential source of energy and momentum in the ionosphere (Yiğit et al., 2016; Kazimirovsky et al., 2003). Solar activity and geomagnetic disturbances also play significant roles with relatively high MDI scores, possibly attributable to the influence of external solar and geomagnetic forcing from above on the terrestrial system (Pedatella, 2016; Yiğit et al., 2016). In this study, we selected the variables above the red dotted

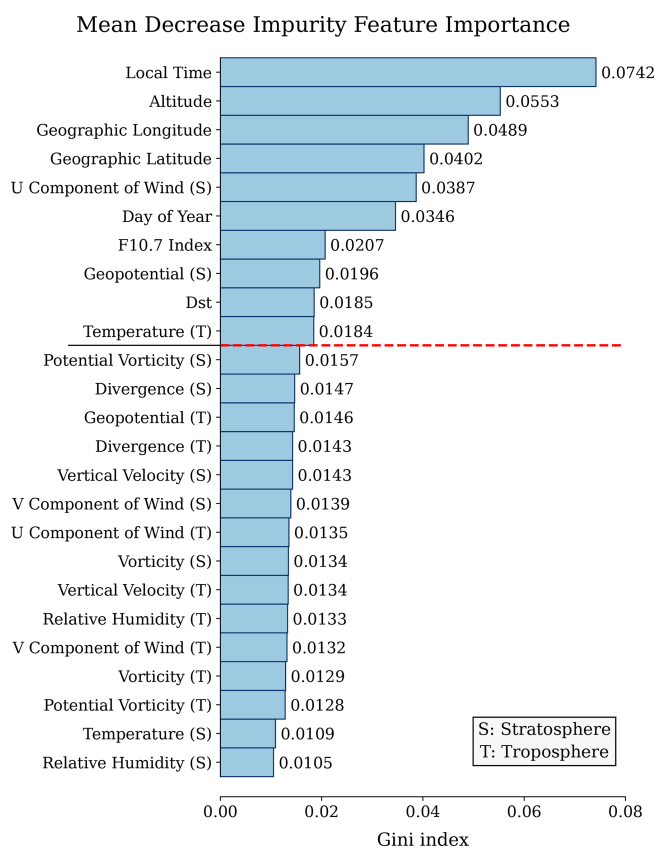


Figure 3. The importance ranking of input variables is based on the mean decrease impurity, which is computed by the random forest regression algorithm. The letters “S” and “T” represent the stratosphere and troposphere, respectively. The part above the red dashed line represents the variables that were selected for subsequent training.

line, as shown in Fig. 3, as the input variables for subsequent SELF-ANN training.

3.2 Results of reconstructing E-region morphology

The results of the global distribution of the test set are presented and discussed in this subsection. In this study, training data were collected from ionospheric scintillation auxiliary data files with scnLv1 format spanning the period 2008 to 2014. Each level-1b file contains continuous S4 data from a single GPS satellite sampled at 50 Hz, yielding one value per second. It provides S4 index and spatiotemporal information in occultation events by calculating the standard deviation of the detrended intensity of received signals normalized to the average signal intensity, covering a range of 80–130 km. In constructing the model, 3 562 999 occultation profile samples were collected, and a validation set of 187 527 samples was utilized to ensure the training’s efficacy. In the test data, we analyzed a total of 937 592 COSMIC RO profiles from 2008 to 2014. The plots presented in

Fig. 4 show the global morphology of Es intensity from observation (Fig. 4a) and SELF-ANN (Fig. 4b). The data are binned in a $2.5^\circ \times 2.5^\circ$ geographic latitude–longitude grid. Each bin corresponds to the average value of all S4max values contained within that bin. To evaluate the regions with significantly higher Es intensity on the globe, we calculated the residual value (mean \pm SD) of observation and the proposed model, depicted by the red boxes with numbers. Inspecting Fig. 4 shows that the predictive results of SELF-ANN exhibit consistency with observations on a large global scale, particularly in capturing the regional distribution feature with higher Es intensity. In general, the distribution of Es demonstrates a strong dependence on the geomagnetic latitude (Yu et al., 2019, 2020, 2021a). For example, the strong magnetization of the electrons near the dip equator results in the lack of Es intensity. The wind shear mechanism which is responsible for sporadic E formation does not exist close to the geomagnetic equator. SELF-ANN provides astonishingly similar predictive results regarding the lack of Es intensity near the geomagnetic equator.

Figure 5 presents global distributions of the seasonal mean intensity of the Es layer for different seasons in the test data. The data were divided into a $2.5^\circ \times 2.5^\circ$ latitude–longitude grid to represent the global distributions. The average S4max values along geographic or geomagnetic latitudes were calculated to depict the latitude distribution. The presented figure demonstrates that the variability of the Es intensity is primarily influenced by seasonal variations, with its maximum in the summer hemisphere and its minimum in the winter hemisphere. The morphology of the Es layers in the four seasons from the proposed model agrees with the observations. The right panels depicting the mean values along the geographic latitude reveal that the Es layer with S4max values greater than 0.5 is mainly distributed at mid-latitudes, as illustrated in Fig. 5g. The Es layer exhibits a weakened presence at the lower latitudes in both hemispheres, and its minimum strength, with S4max values less than 0.2, is located at 60° N latitude in winter. Moreover, the intensity of the Es layer in the northern summer hemisphere is much higher than it is in the southern summer hemisphere. This is probably associated with the lower-thermospheric meridional circulation which flows from the winter to summer hemispheres (Yu et al., 2021b). These shaded blocks with colors indicate the regions with extreme maximum or minimum values for comparison. For example, the deep-blue block in Fig. 5d covers the region near the geomagnetic equator, which exhibits relatively weak Es intensity. The absence of Es intensity along the geomagnetic equator, where the proposed model successfully captures this feature, emphasizes the significant role of geomagnetic control in the formation of the Es layer. As depicted in Fig. 5g and h, the results of the SELF-ANN model display certain disparities when compared to the observations, particularly at high latitudes. A possible explanation for this inconsistency could be the limited availability of training data in these regions (Tian et al., 2022; Yu et al.,

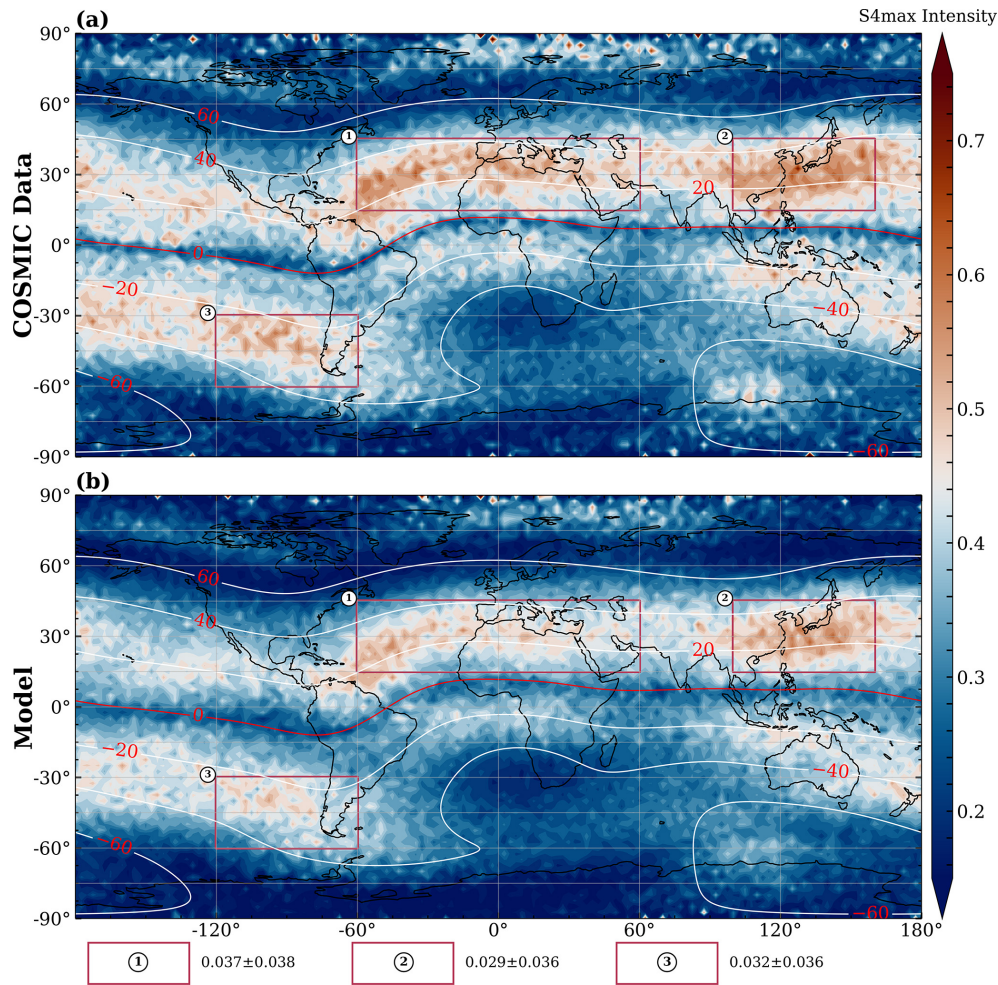


Figure 4. Global distribution of sporadic E intensity from test data. **(a)** COSMIC RO measurements. **(b)** SELF-ANN prediction. The red areas with numbers represent the mean \pm standard deviation of the residuals of the model and observations. The thin white curves signify geomagnetic latitude contours, and the thick red curve is the geomagnetic equator. The geomagnetic latitude was calculated from the International Geomagnetic Reference Field (IGRF). The figures have a latitude–longitude resolution of $2.5^\circ \times 2.5^\circ$.

2022). Overall, the climatological features of Es layers are reproduced by SELF-ANN, indicating its capability to accurately capture the morphology and overall evolution of the ionospheric Es.

Furthermore, a statistical analysis of altitude profiles is presented. Figure 6 shows the altitude–local time, altitude–day of year, altitude–geographic latitude, and altitude–geographic longitude distributions of Es intensity from COSMIC observations and SELF-ANN in the test data. To facilitate visualization, the altitude range of 80–130 km was uniformly divided into 100 bins, as were other variables. Within each bin, the mean value of S4max is represented. In general, the high S4max values exhibit a predominant spatial distribution within the 100–120 km altitude range, as illustrated in Fig. 6a–d. It is noteworthy that the SELF-ANN output has effectively reproduced this distribution feature at the corresponding altitudes. Figure 6a reveals that the alti-

tude distribution of Es varies with local time (LT). Specifically, the intensity of Es is observed to be weaker at approximately 06:00 LT, while it is stronger at approximately 18:00 LT. SELF-ANN demonstrates an ability to successfully capture this diurnal and semidiurnal variation trend in the Es distribution. In addition, the proposed model has reconstructed the annual and semiannual variations found in the seasonal-to-interannual time series of S4max. For instance, in the Northern Hemisphere, the intensity of Es is higher during the summer season compared to the other seasons, as depicted in Fig. 6f. As shown in Fig. 6c, the distribution of Es shows an asymmetry between the Northern Hemisphere and Southern Hemisphere, with the maximum value of S4max observed at mid-latitudes. Moreover, the distribution map of altitude–geographic longitude displays a pattern of wave-like structures (Fig. 6d) (Liu et al., 2021; Yu et al., 2022). These

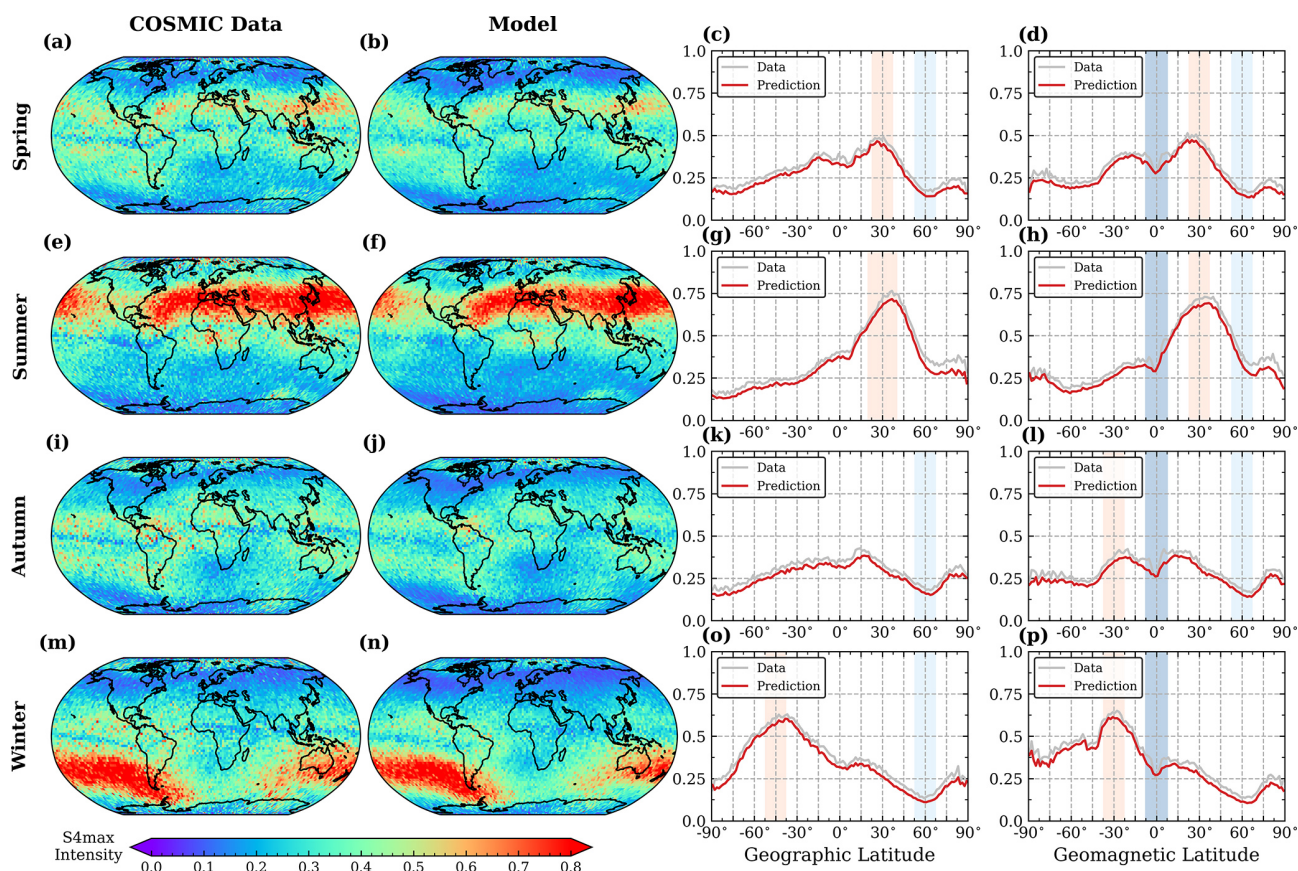


Figure 5. Global distributions of the intensity of the Es layer for different seasons, represented by S4max from COSMIC observations and the SELF-ANN outputs in the period of test data. The different rows in the figure represent spring (March, April, and May), summer (June, July, and August), autumn (September, October, and November), and winter (December, January, and February), respectively. The third and fourth panels in each row represent the mean values along geographic latitude and geomagnetic latitude, respectively. The shaded blocks with colors indicate the regions with extreme maximum or minimum values for the purpose of comparison between COSMIC observations and model predictions.

features of the morphology of Es layers are accurately reconstructed by SELF-ANN.

Prior studies established that the occurrence rate of the Es layer is a commonly utilized metric for statistical analysis of scintillation events (Arras et al., 2008; Yu et al., 2019; Ye et al., 2021). In light of this, we conducted an analysis of amplitude scintillation statistics using data collected by COSMIC satellites and predictions made by SELF-ANN among the test data. To analyze the Es layer's scintillation characteristics, the radio occultation event is considered to include a disturbance, the occurrence of a sporadic E layer, in case the respective S4max intensity exceeds a defined threshold of 0.2 (Arras et al., 2008; Arras and Wickert, 2018; Tian et al., 2022). Figure 7 displays the distribution between altitude, local time, and geomagnetic latitude in relation to the intensity of amplitude scintillation and the occurrence rate of the Es layer derived from observations and predictions, accompanied by the corresponding histogram. The intervals for altitude, local time, and geomagnetic latitude are set to 2 km,

1 h, and 4°, respectively. The occurrence rate is calculated as the ratio of the number of the occultation event with $S4_{\max} \geq 0.2$ to the total number within the corresponding intervals. Within the figure, the blue and gray data points showcase the respective observed and predicted values, whereas the corresponding blue and gray curves highlight the calculated occurrence rate of Es. In general, the COSMIC observations and SELF-ANN predictions are in good agreement. The histograms in Fig. 7a–c present the percentage of RO events with respect to altitude, local time, and geomagnetic latitude as derived from COSMIC data after binning. The majority of S4max index values for scintillation are below 0.5 (Fig. 7d), with the highest occurrence rate of Es observed at an altitude of approximately 110 km (Fig. 7e). At 06:00 LT, the occurrence rate of Es is found to be comparatively low, whereas, at 18:00 LT, it shows an increase (Fig. 7f), which is consistent with the results in Fig. 6i. This can be attributed to the neutral winds controlled by the solar tides in the E region that may dominate and thus govern the diurnal and subdiurnal vari-

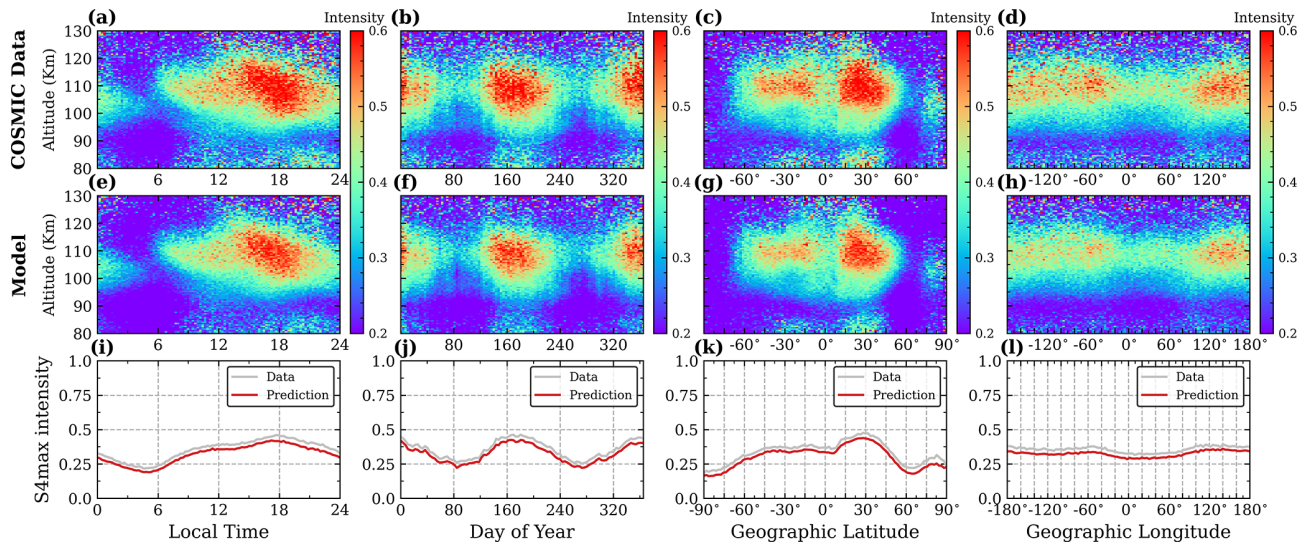


Figure 6. The altitude–local time, altitude–day of year, altitude–latitude, and altitude–longitude distributions of S4max from COSMIC RO measurements in the period of test data. Panels (a–d) and (e–h) correspond to the observed data and the predictions made by SELF-ANN, respectively. Panels (i–l) represent the average intensity of S4max.

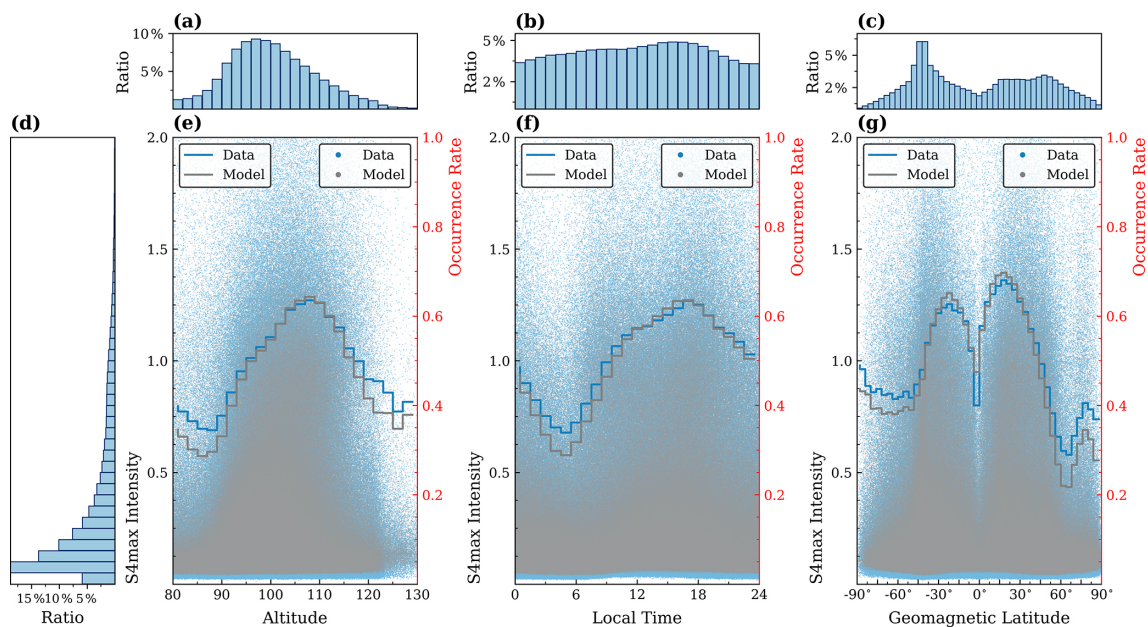


Figure 7. Amplitude scintillation statistic measured by the COSMIC satellites (blue) and predicted by SELF-ANN (gray) between 2013 and 2014. The histograms of RO events observed by COSMIC against altitude (a), local time (b), and geomagnetic latitude (c). (d) The histogram distribution of S4max intensity measured by COSMIC at 80–130 km. The S4max intensity versus altitude (e), local time (f), and geomagnetic latitude (g). The blue (gray) curve represents the occurrence rate of $S4_{\max} \geq 0.2$ from observations (prediction).

ability and descent of the layers through their vertical wind shears (Kazimirovsky et al., 2003; Yiğit et al., 2016). The wind shear theory indicates the close connection between the formation of the Es layer and the geomagnetic latitude for the mid-latitudes (Fig. 7g). The occurrence of Es is comparatively inhibited at the geomagnetic equator due to the ions failing to converge vertically into a layer when the geo-

magnetic field is horizontal. As the geomagnetic inclination rises, the convergence of ions in the vertical direction gradually amplifies, leading to a rise in the occurrence rate of Es. In regions of high geomagnetic latitude, where $\cos I \sim 0$, the vertical velocity of ions is minimal, but the vertical effects of internal waves are effective because of the nature of the geomagnetic field being vertical (Haldoupis, 2011; Plane et al.,

2015; Yu et al., 2019). It is clear that SELF-ANN is capable of reproducing a similar Es occurrence variation against local time like that seen in the observed data and also captures the difference in Es morphology caused by different physical mechanisms, although its occurrence rate predicted by SELF-ANN is lower than that retrieved from the RO data in high-geomagnetic-latitude regions, in part owing to the paucity of data as depicted by the scatter and line plots in Fig. 7e–g.

3.3 Quantitative evaluation and application

To ensure an accurate assessment of the performance of the SELF-ANN model, we conducted quantitative statistical analyses and compared the results to ground-based observations between 2008 and 2014. The histogram of the discrepancies between the observational data obtained from COSMIC and the model predictions proposed in this study is depicted in Fig. 8a. The residual distribution of the test set data indicates a satisfactory agreement between the model and observations. Specifically, approximately 77 % of the data, depicted by the area in the red box in the figure, show a distribution centred around zero. The evaluation metrics, namely ME, MAE, and RMSE, attained values of -0.03 , 0.2 , and 0.33 , respectively. Figure 8b displays the Altman–Bland plots of test cases from COSMIC observations and SELF-ANN predictions, with a least-squares fit to the scattered points shown as a black line. It is apparent that the data points in the plot of differences versus averages form a horizontal V shape, with the open end positioned towards the right, suggesting the feasibility of constructing V-shaped limits (Ludbrook, 2010). The upper confidence limits (UCLs) and lower confidence limits (LCLs) represent the upper and lower bounds, respectively, of the corresponding 95 % confidence limits. The majority of scattered data points fall within the region bounded by the upper and lower confidence limits, which define the range within 95 % differences that can be expected to occur in the scintillation index from the samples (Dewitte et al., 2002; Ludbrook, 2010). This showcases the statistical reliability of the predictive outcomes produced by the presented model. The detailed calculation steps of the Altman–Bland method can be found in Sect. S1.2 in the Supplement.

Figure 8c illustrates a density scatter plot of the scintillation index from COSMIC observations and SELF-ANN outputs with the corresponding correlation coefficient. The correlation analysis between the model outputs and the observations yields a correlation coefficient of 0.607 , indicating a moderate degree of correlation between the two parameters. The p value, which is less than 0.05 , suggests that the correlation coefficient is statistically significant, given the conventional threshold of 0.05 for p values. The statistical findings reveal that the model has a tendency to overestimate smaller values of the scintillation index. This can be attributed to the fact that the model primarily offers a cli-

matological perspective of Es layers, and other electrodynamic processes that potentially influence the vertical movement of ions, such as the neutral wind shear effect, have not yet been accounted for. The results presented in the plot show that the SELF-ANN model is capable of reconstructing Es layers using data from satellite RO measurements, although the prediction of Es layers is severely constrained at present due to a lack of sufficient thermospheric wind data. Furthermore, numerous studies have conducted comparisons between GPS-RO observations of Es layers and ionosonde measurements, revealing that the S4max index exhibits a strong correlation with measurements obtained from worldwide ground-based ionosondes (Emmons et al., 2022; Hodos et al., 2022; Yu et al., 2020; Gooch et al., 2020; Yu et al., 2021a). To ensure the potential practicality of the model and to further evaluate its performance, a comparison was made between the S4max predicted from the SELF-ANN model and the hourly manually scaled critical frequencies of Es layers (f_oEs) obtained from a ground-based ionosonde located in Beijing (40.3° N, 116.2° E). Figure 8d shows the scatter plot of the hourly manually scaled f_oEs from the Beijing ionosonde versus the hourly S4max scintillation index model outputs in the period 2008–2014, selected within a region of $5^\circ \times 5^\circ$ geographical latitudes and longitudes. The red line represents the ordinary least-squares line of best fit, which yields the relation between f_oEs and SELF-ANN outputs $f_oEs = 3.25 + 1.81 \times S4max$ (correlation coefficient: $r = 0.531$, $p \ll 0.05$). The comparison of the predictions with ground-based observations demonstrates the practical applicability and satisfactory predictive performance of the proposed model. Additional quantitative assessment results with other ground-based stations, i.e., Mohe (MH453), Shaoyang (SH427), Sanya (SA418), and Wuhan (WU430) stations, can be accessed in Figs. S1–S4 in the Supplement.

In light of its notable predictive performance that was verified through meticulous comparisons with ground-based observations, a SELF-ANN-based application that is open-source and user-friendly has been established for the purpose of advancing the forecasting of ionospheric irregularities within the space weather community. Figure 9 shows the GUI of the application and its statistical results of predictions. The application initially acquires valid input variables, including year, month, day, hour, latitude, longitude, and altitude, as depicted in Fig. 9a. After that, the tool performs forward propagation within the simplified SELF-ANN model, thereby generating the desired S4max value. The statistical distribution of the mean S4max intensity, as a function of local time and geomagnetic latitude, is illustrated in Fig. 9b and c. The variation of the mean S4max intensity predicted by the application is consistent with the observational data, as evidenced by the previous Fig. 6. Figure 9d presents the distribution of predictive performance metrics for the simplified model across distinct 12-year intervals. The analysis reveals that the model exhibits superior performance within the scope of the training data, en-

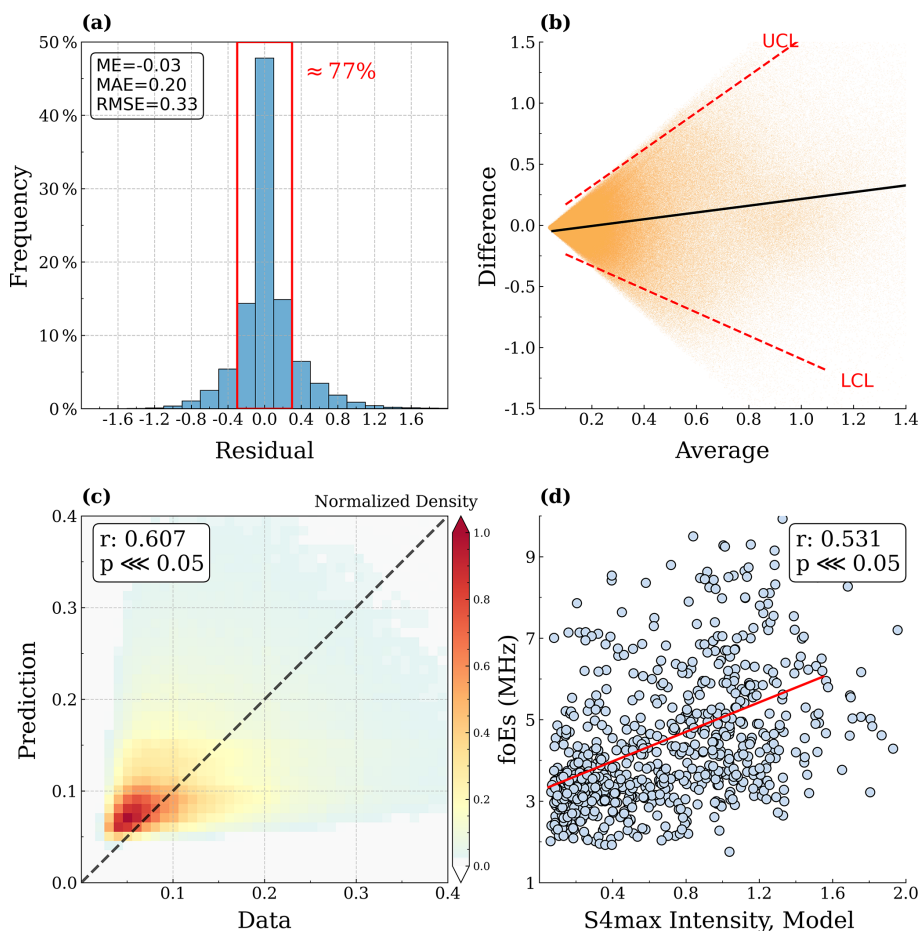


Figure 8. Quantitative assessment results of the SELF-ANN and COSMIC observational data, together with comparative validation of the proposed model with ground-based observations in the test data. **(a)** Histogram of residuals of the amplitude scintillation index between the observation and prediction. The metrics, including mean error (ME), mean absolute error (MAE), and root mean square error (RMSE), are, respectively, marked in the upper left part. **(b)** The Altman–Bland plot of the SELF-ANN prediction in the test data. The UCL and LCL correspond to upper and lower 95 % confidence limits for the Altman–Bland limits of agreement. The black line represents the ordinary least-squares line of best fit. **(c)** Density scatter plot of the scintillation index from COSMIC observations and the model outputs. **(d)** Scatter plot of the hourly manually scaled f_oE_s measured by an ionosonde at Beijing versus the hourly scintillation index from SELF-ANN outputs in the period 2008–2014. The red line represents the ordinary least-squares line of best fit.

compassing the period from 2007 to 2018. The simplified model ignores external driving factors and focuses simply on spatiotemporal information, offering faster computation speed and a wider valid time scope spanning one full solar cycle. As the temporal range expands, the model’s performance demonstrates a corresponding decline. The bidirectional red arrow in Fig. 9d indicates the approximate boundary of the time range in which predictions remain acceptable. Within the 2002–2013 interval, the MAE and RMSE were 0.323 and 0.484, respectively; for 2014–2025, these values were 0.245 and 0.378. The GUI application is based on a simplified version of SELF-ANN that enables users to generate predictions within seconds of providing necessary inputs (<https://github.com/RuleNHao/SELF-ANN>, last access: 16 October 2023). To the best of our knowledge, this is the

first proposed GUI tool of artificial intelligence for prediction in the sporadic E layer. To summarize, the SELF-ANN base tool offers several key advantages, including its ability to provide accurate predictions, its independence of a priori assumptions or theories, and its potential for continued improvement as more input events are added due to the underlying principles of machine learning, making it a valuable contribution to the field of artificial intelligence in the context of space weather prediction.

4 Discussion

We show the existence of an implicit connection between the ionospheric Es layer and external factors (e.g. lower atmosphere, geomagnetic and solar activity), which can be ex-

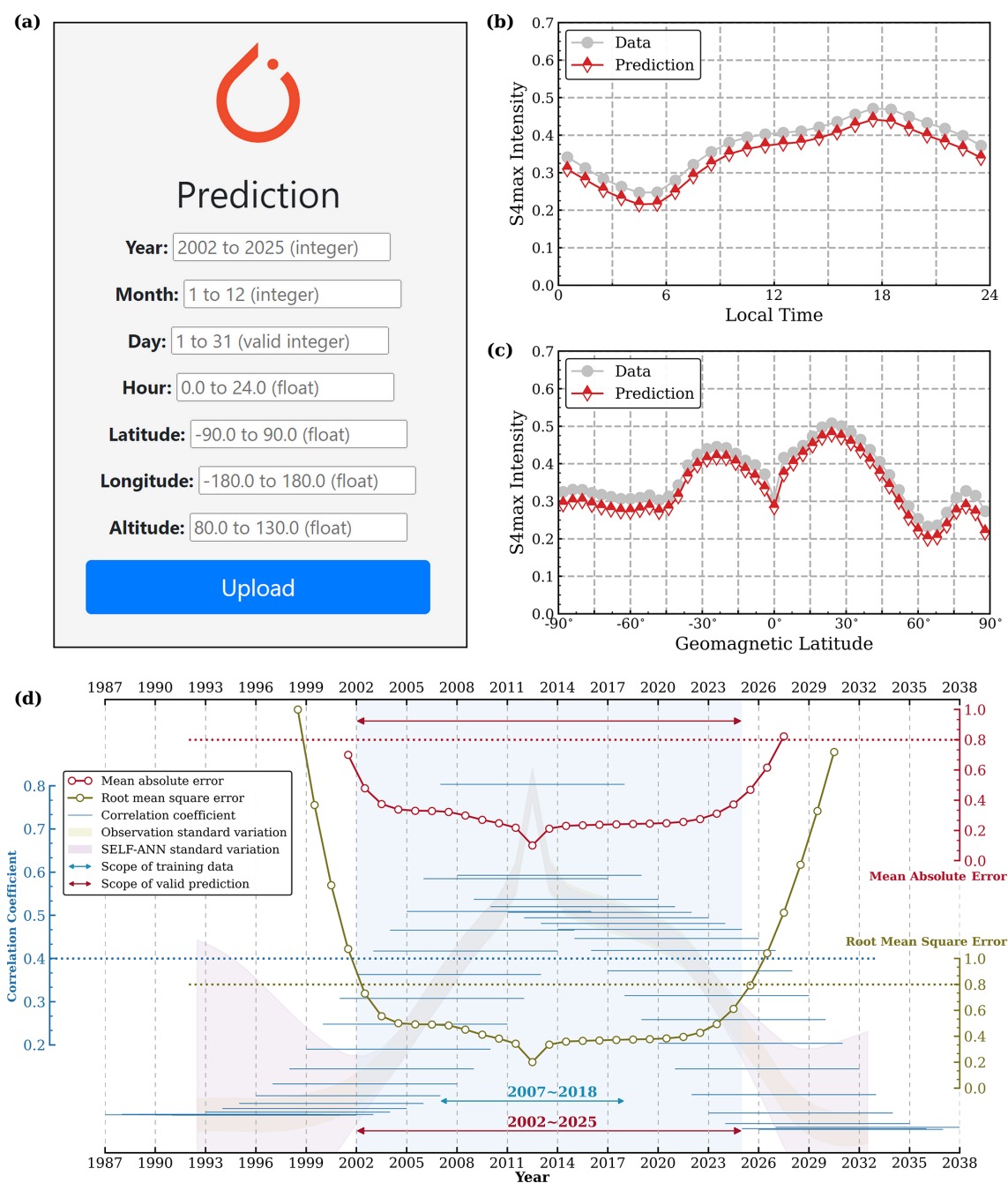


Figure 9. User interface of the SELF-ANN application and its output results. (a) Graphical user interface of the application based on the proposed model. The statistical distribution of mean S4max intensity against local time (b) and geomagnetic latitude (c), comparing SELF-ANN tool outputs and observations. (d) Distribution of predictive performance metrics for the model across distinct 12-year intervals.

tracted via the deep convolutional network. The input feature is obtained by linear interpolation of the spatiotemporal position of the RO event. Each sample consists of local spatial and temporal information, external atmospheric parameters, geomagnetic disturbances, and solar activities, with multi-source data fusion. In this case, we utilized 10 input features of important ranking to train a deep-learning model that ef-

fectively resolves a regression task and reproduces the scintillation index with an exact spatiotemporal location. Furthermore, to our knowledge, this is the first deep-learning-based GUI application developed for the Es-layer reconstruction, which represents a significant contribution to the community in terms of forecasting ionospheric irregularities.

Taking into consideration factors such as data transmission, computational speed, and data timescale, the community-accessible tool is based on a simplified version of SELF-ANN, which provides a wider valid time scope spanning approximately 2002 to 2025 (<https://github.com/RuleNHao/SELF-ANN>). The back-end inference of the simplified model requires only temporal and spatial input parameters, obviating the requirement for other external driving factors (e.g., the ERA5 reanalysis dataset), for the purpose of providing long-term forecast results covering the solar activity cycle with fast computational capabilities. The tool is equipped with a GUI (Fig. 9), which affords users the ability to customize valid time and space parameters and to view the corresponding output. The main advantage of using SELF-ANN is its capacity to provide the S4max scintillation index in an intuitive way through simple parameter configurations without technical barriers. In addition, the consistency of the model prediction and the independent observations from several ground-based ionosondes ensures that the proposed tool is sufficiently generalized and reliable.

Our model architecture was motivated by ResNet, used for regression tasks. A total of 4 691 412 available data samples was extracted from COSMIC occultation events, each accompanied by corresponding variables representing external driving factors. The input variables undergo a conversion process wherein they are transformed into the one-dimensional input array. Since an increase in data points in the input space (e.g., using all the available lower-atmospheric data) did increase the computational needs above the available resources, we restricted this to the maximal depth of the first input layer. Therefore, we utilized the random forest regression algorithm, a conventional machine-learning technique, to perform initial screening of the data. This approach not only facilitates the identification of more efficient input information for model training, but also provides a degree of insight into the interpretability of the data. No further attempts were made to compare different architectures. The main goal of our work was to demonstrate that the implicit mapping relationships contained between external factors (e.g., lower wind data, temperature, solar activity) and the ionospheric Es layer can be extracted by deep-learning networks. Future research should focus on the further optimization of this approach, for instance by integrating the wind data in the E region that are crucial to forming the Es, modifying filter settings, and adjusting network architectures. In addition, the exploration of model interpretability is an important issue for future work.

This study builds upon the research conducted by Tian et al. (2022) and aims to extend their findings. Compared to the Tian et al. (2022) findings, our results have demonstrated significant advancements. By treating each radio occultation event as a sample, we have eliminated the error caused by interpolation and improved the accuracy of the model. Furthermore, we have briefly explored the importance of input information in explaining the predictive capability of the model,

utilizing the random forest approach. This finding provides valuable insight into the interpretation of the model, facilitating a more comprehensive understanding of its predictive power. The comparison with ground-based ionosonde observations provides strong evidence for the robustness of the model and its potential for practical applications. In Figs. 5 and 7, the analysis reveals that the Es layers at high altitudes and latitudes exhibit significant disagreements between the model outputs and the observational data, notwithstanding the model's ability to reconstruct the morphology of the Es layers. A limitation of the model is its primary focus on describing the meridional migration of Es layers within the mid-latitudinal range, resulting in a deficient representation of the high-altitude and high-latitude Es layers. Therefore, we will address the shortcomings of the model in future work by including more input factors (e.g., strong wind shears, fast solar wind streams, equatorial electrojet current plasma, atmosphere perturbations in the E region, and variations in meteor flux).

In summary, an implicit relationship exists between external driving factors and ionospheric irregularities, and deep convolutional networks can extract latent features from actual observations beyond traditional methods. Deep nets might also substitute or complement human-guided feature extraction and knowledge discovery in other specialties where spatiotemporal data are ubiquitous, including remote-sensing and geographic information science, geodesy, atmospheric science, hydrological earth science, and planetary science. This approach can also be applied to distinguish extreme weather events and is expected to contribute to the prediction of space weather.

5 Conclusions

In this research, we have introduced a new tool, referred to as SELF-ANN (Sporadic E Layer Forecast using Artificial Neural Networks), which has been purposefully designed to forecast the ionospheric Es layer by implementing a multisource data fusion approach based on deep-learning techniques. The model architecture of our proposed approach is derived from ResNet, with several modifications made to align with the dataset for both accuracy and robustness. The training dataset used in this study consists of ionospheric Es-layer data from COSMIC RO measurements, atmospheric perturbation information from ERA5 data, the collected geomagnetic disturbances, and solar activities, among others. We performed an initial exploratory analysis of the interpretability for all the input data using a conventional machine-learning method, with a specific focus on random forest regression. The findings suggest that local time, altitude, and geographic coordinates play a more significant role in the reconstruction of the Es layer in comparison to other parameters. Following a ranking of feature importance, we identified and selected several highly important features, including the spatiotempo-

ral information, zonal wind, temperature, geopotential, geomagnetic disturbances, and solar activity, from all the candidate input information for use in model training. The well-trained model has the capability to effectively capture the implicit relationships between external driving factors, such as local atmospheric variations, and the ionospheric irregularities. Moreover, the high-level features of large-scale seasonal variations in Es layers are also efficiently learned, verifying the feasibility, effectiveness, and generalization capability of the proposed framework.

Multiple quantitative evaluation metrics were employed to evaluate the performance of the model. The evaluation resulted in achieving a MAE value of 0.2, RMSE of 0.33, and correlation coefficient of 0.607, indicating that the model exhibits superior predictive performance. In order to assess the generalization ability of the proposed model, ionosonde data collected from Beijing, China, were utilized. The analysis demonstrated that the correlation coefficient between the hourly f_oE_s and model outputs is 0.531, which ensures the feasibility of practical applications. Therefore, we develop for the first time a web-based open-source ionospheric E-region forecast application that is user-friendly and can potentially aid researchers in their investigation of ionospheric irregularities. The proposed tool is expected to make a significant contribution to not only the prediction of extreme space weather events, but also to opening up new possibilities for the application of artificial intelligence in upper-atmospheric and ionospheric physics.

Code and data availability. The reanalysis data used for part of the input in this study are available from ECMWF Reanalysis v5 (ERA5) (<https://doi.org/10.24381/cds.bd0915c6>, Hersbach et al., 2023). The COSMIC RO data were downloaded from the FORMOSAT-3/Constellation Observing System for Meteorology Ionosphere and Climate (COSMIC-1 (<https://doi.org/10.5065/ZD80-KD74>, UCAR COSMIC Program, 2022)). Geomagnetic and solar activity data were obtained from the OMNI Goddard Space Physics Data Facility (<https://omniweb.gsfc.nasa.gov/>, King and Papitashvili, 2005). The ionosonde data are available from the Data Centre for Meridian Space Weather Monitoring Project (<https://data.meridianproject.ac.cn/data-directory/>, Meridian Space Weather Monitoring Project, 2023, log-in required) and the National Space Science Data Center (National Science and Technology Infrastructure of China) (<http://www.nssdc.ac.cn>, National Space Science Data Center, 2023, log-in required). The GUI application and source code used in this work can be found in GitHub (<https://doi.org/10.5281/zenodo.10016010>, Tian et al., 2023).

Supplement. The supplement related to this article is available online at: <https://doi.org/10.5194/acp-23-13413-2023-supplement>.

Author contributions. PT designed the study and wrote the manuscript. BY provided early ideas and the manually scaled iono-

spheric observation. BY and PT contributed to the comments on an early version of the manuscript. XX and JW contributed to the discussion of the results and the preparation of the manuscript. HY performed part of the analysis results. HY and TC provided an advisory role in analyzing the data. All the authors discussed the results and commented on the manuscript at all stages.

Competing interests. The contact author has declared that none of the authors has any competing interests.

Disclaimer. Publisher's note: Copernicus Publications remains neutral with regard to jurisdictional claims made in the text, published maps, institutional affiliations, or any other geographical representation in this paper. While Copernicus Publications makes every effort to include appropriate place names, the final responsibility lies with the authors.

Acknowledgements. We acknowledge the COSMIC Data Analysis and Archive Center (CDAAC) for providing COSMIC RO data. Moreover, we particularly thank the European Centre for Medium-Range Weather Forecasts for providing the ERA5 reanalysis data. We acknowledge use of the NASA and GSFC Space Physics Data Facility's OMNIWeb (or CDAWeb or ftp) service and OMNI data. The authors acknowledge the Chinese Meridian Project, the Solar-Terrestrial Environment Research Network, the Geophysics Center, the National Earth System Science Data Center at BNOSE, IGGCAS, and the National Space Science Data Center (National Science and Technology Infrastructure of China) for providing the ionosonde data. The training of the model in this paper was done on the supercomputing system at the Supercomputing Center of the University of Science and Technology of China.

Financial support. This work is supported by the National Natural Science Foundation of China (grant nos. 42125402, 42188101, and 42074181), the Project of Stable Support for Youth Team in Basic Research Field, CAS (YSBR-018), the National Key R&D Program of China (grant no. 2022YFF0503703), the Innovation Program for Quantum Science and Technology (grant no. 2021ZD0300300), the Frontier Scientific Research Program of the Deep Space Exploration Laboratory (grant no. 2022-QYKYJH-ZYTS-016), and the Joint Open Fund of Mengcheng National Geophysical Observatory (grant no. MENGO-202207). Jianfei Wu was funded by the Fundamental Research Funds for the Central Universities (grant no. WK3420000020).

Review statement. This paper was edited by John Plane and reviewed by two anonymous referees.

References

Altman, D. G. and Bland, J. M.: Measurement in medicine: the analysis of method comparison studies, *J. Roy. Stat. Soc. D-Stat.*, 32, 307–317, 1983.

- Anthes, R. A., Bernhardt, P., Chen, Y., Cucurull, L., Dymond, K., Ector, D., Healy, S., Ho, S.-P., Hunt, D., and Kuo, Y.-H.: The COSMIC/FORMOSAT-3 mission: Early results, *B. Am. Meteorol. Soc.*, 89, 313–334, <https://doi.org/10.1175/BAMS-89-3-313>, 2008.
- Arras, C. and Wickert, J.: Estimation of ionospheric sporadic E intensities from GPS radio occultation measurements, *J. Atmos. Sol.-Terr. Phys.*, 171, 60–63, 2018.
- Arras, C., Wickert, J., Beyerle, G., Heise, S., Schmidt, T., and Jacobi, C.: A global climatology of ionospheric irregularities derived from GPS radio occultation, *Geophys. Res. Lett.*, 35, L14809, <https://doi.org/10.1029/2008GL034158>, 2008.
- Arras, C., Jacobi, C., and Wickert, J.: Semidiurnal tidal signature in sporadic E occurrence rates derived from GPS radio occultation measurements at higher midlatitudes, *Ann. Geophys.*, 27, 2555–2563, <https://doi.org/10.5194/angeo-27-2555-2009>, 2009.
- Bengio, Y., Simard, P., and Frasconi, P.: Learning long-term dependencies with gradient descent is difficult, *IEEE T. Neural Netw.*, 5, 157–166, 1994.
- Bilitza, D., Pezzopane, M., Truhlik, V., Altadill, D., Reinisch, B. W., and Pignalberi, A.: The International Reference Ionosphere model: A review and description of an ionospheric benchmark, *Rev. Geophys.*, 60, e2022RG000792, <https://doi.org/10.1029/2022RG000792>, 2022.
- Bowling, M. and Veloso, M.: Multiagent learning using a variable learning rate, *Artif. Intell.*, 136, 215–250, 2002.
- Breiman, L.: Random forests, *Machine Learn.*, 45, 5–32, 2001.
- Breiman, L.: Classification and regression trees, Routledge, <https://doi.org/10.1201/9781315139470>, 2017.
- Briggs, B. and Parkin, I.: On the variation of radio star and satellite scintillations with zenith angle, *J. Atmos. Terr. Phys.*, 25, 339–366, 1963.
- Carter, L. N. and Forbes, J. M.: Global transport and localized layering of metallic ions in the upper atmosphere, *Ann. Geophys.*, 17, 190–209, <https://doi.org/10.1007/s00585-999-0190-6>, 1999.
- Chapman, S.: The absorption and dissociative or ionizing effect of monochromatic radiation in an atmosphere on a rotating earth, *P. Phys. Soc.*, 43, 26–45, <https://doi.org/10.1088/0959-5309/43/1/305>, 1931a.
- Chapman, S.: The absorption and dissociative or ionizing effect of monochromatic radiation in an atmosphere on a rotating earth part II. Grazing incidence, *P. Phys. Soc.*, 43, 483–501, <https://doi.org/10.1088/0959-5309/43/5/302>, 1931b.
- Chu, Y.-H., Wang, C., Wu, K., Chen, K., Tzeng, K., Su, C.-L., Feng, W., and Plane, J.: Morphology of sporadic E layer retrieved from COSMIC GPS radio occultation measurements: Wind shear theory examination, *J. Geophys. Res.-Space*, 119, 2117–2136, 2014.
- Couronné, R., Probst, P., and Boulesteix, A.-L.: Random forest versus logistic regression: a large-scale benchmark experiment, *BMC bioinformatics*, 19, 1–14, 2018.
- Dewitte, K., Fierens, C., Stockl, D., and Thienpont, L. M.: Application of the Bland–Altman plot for interpretation of method-comparison studies: a critical investigation of its practice, *Clin. Chem.*, 48, 799–801, 2002.
- Djuth, F., Zhang, L., Livneh, D., Seker, I., Smith, S., Sulzer, M., Mathews, J., and Walterscheid, R.: Arecibo’s thermospheric gravity waves and the case for an ocean source, *J. Geophys. Res.-Space*, 115, A08305, <https://doi.org/10.1029/2009JA014799>, 2010.
- Emmons, D. J., Wu, D. L., and Swarnalingam, N.: A Statistical Analysis of Sporadic-E Characteristics Associated with GNSS Radio Occultation Phase and Amplitude Scintillations, *Atmosphere*, 13, 2098, <https://doi.org/10.3390/atmos13122098>, 2022.
- Giamalaki, K., Beaulieu, C., and Prochaska, J.: Assessing predictability of marine heatwaves with random forests, *Geophys. Res. Lett.*, 49, e2022GL099069, <https://doi.org/10.1029/2022GL099069>, 2022.
- Glorot, X. and Bengio, Y.: Understanding the difficulty of training deep feedforward neural networks, in: Proceedings of the thirteenth international conference on artificial intelligence and statistics, JMLR Workshop and Conference Proceedings, 13–15 May 2010, Chia Laguna Resort, Sardinia, Italy, 249–256, 2010.
- Goncharenko, L., Chau, J., Liu, H.-L., and Coster, A.: Unexpected connections between the stratosphere and ionosphere, *Geophys. Res. Lett.*, 37, L10101, <https://doi.org/10.1029/2010GL043125>, 2010.
- Gooch, J. Y., Colman, J. J., Nava, O. A., and Emmons, D. J.: Global ionosonde and GPS radio occultation sporadic-E intensity and height comparison, *J. Atmos. Sol.-Terr. Phys.*, 199, 105200, <https://doi.org/10.1016/j.jastp.2020.105200>, 2020.
- Haldoupis, C.: A tutorial review on sporadic E layers, in: *Aeronomy of the Earth’s Atmosphere and Ionosphere*, edited by: Abdu, M. and Pancheva, D., 381–394, Vol. 2, Springer, Dordrecht, https://doi.org/10.1007/978-94-007-0326-1_29, 2011.
- Ham, Y.-G., Kim, J.-H., and Luo, J.-J.: Deep learning for multi-year ENSO forecasts, *Nature*, 573, 568–572, 2019.
- He, K., Zhang, X., Ren, S., and Sun, J.: Deep residual learning for image recognition, in: Proceedings of the IEEE conference on computer vision and pattern recognition (CVPR), Las Vegas, NV, USA, 770–778, <https://doi.org/10.1109/CVPR.2016.90>, 2016.
- Hersbach, H., Bell, B., Berrisford, P., et al.: The ERA5 global reanalysis, *Q. J. Roy. Meteor. Soc.*, 146, 1999–2049, <https://doi.org/10.1002/qj.3803>, 2020.
- Hersbach, H., Bell, B., Berrisford, P., Biavati, G., Horányi, A., Muñoz Sabater, J., Nicolas, J., Peubey, C., Radu, R., Rozum, I., Schepers, D., Simmons, A., Soci, C., Dee, D., and Thépaut, J.-N.: ERA5 hourly data on pressure levels from 1940 to present, Copernicus Climate Change Service (C3S) Climate Data Store (CDS) [data set], <https://doi.org/10.24381/cds.bd0915c6>, 2023.
- Hodos, T. J., Nava, O. A., Dao, E. V., and Emmons, D. J.: Global sporadic-E occurrence rate climatology using GPS radio occultation and ionosonde data, *J. Geophys. Res.-Space*, 127, e2022JA030795, <https://doi.org/10.1029/2022JA030795>, 2022.
- Ioffe, S. and Szegedy, C.: Batch normalization: Accelerating deep network training by reducing internal covariate shift, in: International conference on machine learning, 6–11 July 2015, Lille, France, 448–456, pmlr, 2015.
- Jin, H., Miyoshi, Y., Fujiwara, H., Shinagawa, H., Terada, K., Terada, N., Ishii, M., Otsuka, Y., and Saito, A.: Vertical connection from the tropospheric activities to the ionospheric longitudinal structure simulated by a new Earth’s whole atmosphere-ionosphere coupled model, *J. Geophys. Res.-Space*, 116, A01316, <https://doi.org/10.1029/2010JA015925>, 2011.
- Johnson, E. and Heelis, R.: Characteristics of ion velocity structure at high latitudes during steady southward interplanetary magnetic field conditions, *J. Geophys. Res.-Space*, 110, A12301, <https://doi.org/10.1029/2005JA011130>, 2005.

- Kazimirovsky, E., Herraiz, M., and De la Morena, B.: Effects on the ionosphere due to phenomena occurring below it, *Surv. Geophys.*, 24, 139–184, 2003.
- Kim, T.-Y. and Cho, S.-B.: Predicting residential energy consumption using CNN-LSTM neural networks, *Energy*, 182, 72–81, 2019.
- King, J. H. and Papitashvili, N. E.: Solar wind spatial scales in and comparisons of hourly Wind and ACE plasma and magnetic field data, *J. Geophys. Res.*, 110, A02209, <https://doi.org/10.1029/2004JA010649>, 2005 (data available at: <https://omniweb.gsfc.nasa.gov/>, last access: 16 October 2023).
- Kirkwood, S. and Nilsson, H.: High-latitude sporadic-E and other thin layers—the role of magnetospheric electric fields, *Space Sci. Rev.*, 91, 579–613, 2000.
- LeCun, Y., Bengio, Y., and Hinton, G.: Deep learning, *Nature*, 521, 436–444, 2015.
- Lei, J., Syndergaard, S., Burns, A. G., Solomon, S. C., Wang, W., Zeng, Z., Roble, R. G., Wu, Q., Kuo, Y.-H., Holt, J. M., Zhang, S.-R., Hysell, D. L., Rodrigues, F. S., and Lin, C. H.: Comparison of COSMIC ionospheric measurements with ground-based observations and model predictions: Preliminary results, *J. Geophys. Res.-Space*, 112, A07308, <https://doi.org/10.1029/2006JA012240>, 2007.
- Lei, J., Thayer, J. P., Forbes, J. M., Wu, Q., She, C., Wan, W., and Wang, W.: Ionosphere response to solar wind high-speed streams, *Geophys. Res. Lett.*, 35, L19105, <https://doi.org/10.1029/2008GL035208>, 2008.
- Li, G., Ning, B., Otsuka, Y., Abdu, M. A., Abadi, P., Liu, Z., Spogli, L., and Wan, W.: Challenges to equatorial plasma bubble and ionospheric scintillation short-term forecasting and future aspects in east and southeast Asia, *Surv. Geophys.*, 42, 201–238, 2021.
- Licata, R. J., Mehta, P. M., Tobiska, W. K., and Huzurbazar, S.: Machine-learned HASDM thermospheric mass density model with uncertainty quantification, *Space Weather*, 20, e2021SW002915, <https://doi.org/10.1029/2021SW002915>, 2022.
- Liu, Y., Duffy, K., Dy, J. G., and Ganguly, A. R.: Explainable deep learning for insights in El Niño and river flows, *Nat. Commun.*, 14, 339, 2023.
- Liu, Z., Fang, H., Yue, X., and Lyu, H.: Wavenumber-4 Patterns of the Sporadic E Over the Middle-and Low-Latitudes, *J. Geophys. Res.-Space*, 126, e2021JA029238, <https://doi.org/10.1029/2021JA029238>, 2021.
- Ludbrook, J.: Confidence in Altman–Bland plots: a critical review of the method of differences, *Clin. Exp. Pharmacol. P.*, 37, 143–149, 2010.
- Lühr, H., Alken, P., and Zhou, Y.-L.: The equatorial electrojet, in: *Ionosphere Dynamics and Applications*, edited by: Huang, C., Lu, G., Zhang, Y., and Paxton, L. J., *Geophysical Monograph Series*, 281–299, <https://doi.org/10.1002/9781119815617.ch12>, 2021.
- MacDougall, J., Jayachandran, P., and Plane, J.: Polar cap Sporadic-E: part 1, observations, *J. Atmos. Sol.-Terr. Phys.*, 62, 1155–1167, 2000.
- Mathews, J.: Sporadic E: current views and recent progress, *J. Atmos. Sol.-Terr. Phys.*, 60, 413–435, 1998.
- Matsushita, S. and Reddy, C.: A study of blanketing sporadic E at middle latitudes, *J. Geophys. Res.*, 72, 2903–2916, 1967.
- Meridian Space Weather Monitoring Project: Digital ionosonde data, CMP [data set], <https://data.meridianproject.ac.cn/data-directory/>, last access: 16 October 2023.
- Nair, V. and Hinton, G. E.: Rectified linear units improve restricted boltzmann machines, in: *Proceedings of the 27th international conference on machine learning (ICML-10)*, 21–24 June 2010, Haifa, Israel, 807–814, 2010.
- National Space Science Data Center: Digital ionosonde data, NSSDC [data set], <http://www.nssdc.ac.cn>, last access: 16 October 2023.
- Nygren, T., Jalonen, L., Oksman, J., and Turunen, T.: The role of electric field and neutral wind direction in the formation of sporadic E-layers, *J. Atmos. Terr. Phys.*, 46, 373–381, 1984.
- Ogawa, T., Suzuki, A., and Kunitake, M.: Spatial distribution of mid-latitude sporadic E scintillations in summer daytime, *Radio Sci.*, 24, 527–538, 1989.
- Oshiro, T. M., Perez, P. S., and Baranaukas, J. A.: How many trees in a random forest?, in: *Machine Learning and Data Mining in Pattern Recognition: 8th International Conference, MLDM 2012*, Berlin, Germany, 13–20 July 2012. *Proceedings 8*, pp. 154–168, Springer, 2012.
- Papitashvili, N. E. and King, J. H.: OMNI Hourly Data Set, NASA Space Physics Data Facility [data set], <https://doi.org/10.48322/1SHR-HT18>, 2020.
- Pavelyev, A., Liou, Y., Wickert, J., Schmidt, T., Pavelyev, A., and Liu, S.-F.: Effects of the ionosphere and solar activity on radio occultation signals: Application to CHALLENGING Minisatellite Payload satellite observations, *J. Geophys. Res.-Space*, 112, A06326, <https://doi.org/10.1029/2006JA011625>, 2007.
- Pedatella, N. M.: Impact of the lower atmosphere on the ionosphere response to a geomagnetic superstorm, *Geophys. Res. Lett.*, 43, 9383–9389, 2016.
- Plane, J. M.: Cosmic dust in the earth’s atmosphere, *Chem. Soc. Rev.*, 41, 6507–6518, 2012.
- Plane, J. M., Feng, W., and Dawkins, E. C.: The mesosphere and metals: Chemistry and changes, *Chem. Rev.*, 115, 4497–4541, 2015.
- Priyadarshi, S.: A review of ionospheric scintillation models, *Surv. Geophys.*, 36, 295–324, 2015.
- Qian, L., Burns, A. G., Emery, B. A., Foster, B., Lu, G., Maute, A., Richmond, A. D., Roble, R. G., Solomon, S. C., and Wang, W.: The NCAR TIE-GCM: A community model of the coupled thermosphere/ionosphere system, in: *Modeling the ionosphere–thermosphere system*, edited by: Huba, J., Schunk, R., and Khazanov, G., 73–83, <https://doi.org/10.1002/9781118704417.ch7>, 2014.
- Raghavarao, R., Patra, A., and Sripathi, S.: Equatorial E region irregularities: A review of recent observations, *J. Atmos. Sol.-Terr. Phys.*, 64, 1435–1443, 2002.
- Reichstein, M., Camps-Valls, G., Stevens, B., Jung, M., Denzler, J., and Carvalhais, N.: Deep learning and process understanding for data-driven Earth system science, *Nature*, 566, 195–204, 2019.
- Resende, L. C. A., Batista, I. S., Denardini, C. M., Batista, P. P., Carrasco, A. J., de Fátima Andrioli, V., and Moro, J.: Simulations of blanketing sporadic E-layer over the Brazilian sector driven by tidal winds, *J. Atmos. Sol.-Terr. Phys.*, 154, 104–114, 2017.
- Roble, R. and Ridley, E.: A thermosphere-ionosphere-mesosphere-electrodynamics general circulation model (TIME-GCM):

- Equinox solar cycle minimum simulations (30–500 km), *Geophys. Res. Lett.*, 21, 417–420, 1994.
- Rocken, C., Ying-Hwa, K., Schreiner, W. S., Hunt, D., Sokolovskiy, S., and McCormick, C.: COSMIC system description, *Terr. Atmos. Ocean. Sci.*, 11, 21–52, 2000.
- Ruder, S.: An overview of gradient descent optimization algorithms, arXiv [preprint], arXiv:1609.04747, 2016.
- Salcedo-Sanz, S., Ghamisi, P., Piles, M., Werner, M., Cuadra, L., Moreno-Martínez, A., Izquierdo-Verdiguier, E., Muñoz-Marí, J., Mosavi, A., and Camps-Valls, G.: Machine learning information fusion in Earth observation: A comprehensive review of methods, applications and data sources, *Inform. Fusion*, 63, 256–272, 2020.
- Schmidhuber, J.: Deep learning in neural networks: An overview, *Neural Networks*, 61, 85–117, 2015.
- Schreiner, W., Rocken, C., Sokolovskiy, S., Syndergaard, S., and Hunt, D.: Estimates of the precision of GPS radio occultations from the COSMIC/FORMOSAT-3 mission, *Geophys. Res. Lett.*, 34, L04808, <https://doi.org/10.1029/2006GL027557>, 2007.
- Schreiner, W., Sokolovskiy, S., Hunt, D., Rocken, C., and Kuo, Y.-H.: Analysis of GPS radio occultation data from the FORMOSAT-3/COSMIC and Metop/GRAS missions at CDAAC, *Atmos. Meas. Tech.*, 4, 2255–2272, <https://doi.org/10.5194/amt-4-2255-2011>, 2011.
- Shinagawa, H., Miyoshi, Y., Jin, H., and Fujiwara, H.: Global distribution of neutral wind shear associated with sporadic E layers derived from GAIA, *J. Geophys. Res.-Space*, 122, 4450–4465, 2017.
- Shinagawa, H., Tao, C., Jin, H., Miyoshi, Y., and Fujiwara, H.: Numerical prediction of sporadic E layer occurrence using GAIA, *Earth Planets Space*, 73, 1–18, 2021.
- Silver, D., Schrittwieser, J., Simonyan, K., Antonoglou, I., Huang, A., Guez, A., Hubert, T., Baker, L., Lai, M., Bolton, A., Chen, Y., Lillicrap, T., Hui, F., Sifre, L., van den Driessche, G., Graepel, T., and Hassabis, D.: Mastering the game of go without human knowledge, *Nature*, 550, 354–359, 2017.
- Simonyan, K. and Zisserman, A.: Very deep convolutional networks for large-scale image recognition, arXiv [preprint], arXiv:1409.1556, 2014.
- Sokolovskiy, S., Schreiner, W., Zeng, Z., Hunt, D., Lin, Y.-C., and Kuo, Y.-H.: Observation, analysis, and modeling of deep radio occultation signals: Effects of tropospheric ducts and interfering signals, *Radio Sci.*, 49, 954–970, 2014.
- Svetnik, V., Liaw, A., Tong, C., Culberson, J. C., Sheridan, R. P., and Feuston, B. P.: Random forest: a classification and regression tool for compound classification and QSAR modeling, *J. Chem. Inf. Comp. Sci.*, 43, 1947–1958, 2003.
- Szegedy, C., Liu, W., Jia, Y., Sermanet, P., Reed, S., Anguelov, D., Erhan, D., Vanhoucke, V., and Rabinovich, A.: Going deeper with convolutions, in: Proceedings of the IEEE conference on computer vision and pattern recognition, Boston, MA, USA, 1–9, <https://doi.org/10.1109/CVPR.2015.7298594>, 2015.
- Thayer, J. P. and Semeter, J.: The convergence of magnetospheric energy flux in the polar atmosphere, *J. Atmos. Sol.-Terr. Phys.*, 66, 807–824, 2004.
- Tian, P., Yu, B., Ye, H., Xue, X., Wu, J., and Chen, T.: Estimation Model of Global Ionospheric Irregularities: An Artificial Intelligence Approach, *Space Weather*, 20, e2022SW003160, <https://doi.org/10.1029/2022SW003160>, 2022.
- Tian, P., Yu, B., Ye, H., Xue, X., Wu, J., and Chen, T.: Ionospheric Irregularities Reconstruction Using Multi-Source Data Fusion via Deep Learning, Zenodo [code], <https://doi.org/10.5281/zenodo.10016010>, 2023.
- Titheridge, J.: Modelling the peak of the ionospheric E-layer, *J. Atmos. Sol.-Terr. Phys.*, 62, 93–114, 2000.
- Tsai, L.-C., Su, S.-Y., Liu, C.-H., Schuh, H., Wickert, J., and Alizadeh, M. M.: Global morphology of ionospheric sporadic E layer from the FormoSat-3/COSMIC GPS radio occultation experiment, *GPS Solutions*, 22, 1–12, 2018.
- UCAR COSMIC Program: COSMIC-1 Data Products, UCAR/N-CAR – COSMIC [data set], <https://doi.org/10.5065/ZD80-KD74>, 2022.
- Vadas, S. L. and Liu, H.-I.: Generation of large-scale gravity waves and neutral winds in the thermosphere from the dissipation of convectively generated gravity waves, *J. Geophys. Res.-Space*, 114, A10310, <https://doi.org/10.1029/2009JA014108>, 2009.
- Weber, E., Tsunoda, R., Buchau, J., Sheehan, R., Strickland, D., Whiting, W., and Moore, J.: Coordinated measurements of auroral zone plasma enhancements, *J. Geophys. Res.-Space*, 90, 6497–6513, 1985.
- Whitehead, J.: The formation of the sporadic-E layer in the temperate zones, *J. Atmos. Terr. Phys.*, 20, 49–58, 1961.
- Whitehead, J.: Production and prediction of sporadic E, *Rev. Geophys.*, 8, 65–144, 1970.
- Whitehead, J.: Recent work on mid-latitude and equatorial sporadic-E, *J. Atmos. Terr. Phys.*, 51, 401–424, 1989.
- Wu, J., Feng, W., Liu, H.-L., Xue, X., Marsh, D. R., and Plane, J. M. C.: Self-consistent global transport of metallic ions with WACCM-X, *Atmos. Chem. Phys.*, 21, 15619–15630, <https://doi.org/10.5194/acp-21-15619-2021>, 2021.
- Ye, H., Xue, X., Yu, T., Sun, Y.-Y., Yi, W., Long, C., Zhang, W., and Dou, X.: Ionospheric F-layer scintillation variabilities over the American sector during sudden stratospheric warming events, *Space Weather*, 19, e2020SW002703, <https://doi.org/10.1029/2020SW002703>, 2021.
- Ye, H., Yi, W., Zhou, B., Wu, J., Yu, B., Tian, P., Wang, J., Long, C., Lu, M., Xue, X., Chen, T., and Dou, X.: Multi-Instrumental Observations of Midlatitude Plasma Irregularities over Eastern Asia during a Moderate Magnetic Storm on 16 July 2003, *Remote Sens.-Basel*, 15, 1160, <https://doi.org/10.3390/rs15041160>, 2023.
- Yiğit, E., Knížová, P. K., Georgieva, K., and Ward, W.: A review of vertical coupling in the Atmosphere–Ionosphere system: Effects of waves, sudden stratospheric warmings, space weather, and of solar activity, *J. Atmos. Sol.-Terr. Phys.*, 141, 1–12, 2016.
- Yu, B., Xue, X., Yue, X., Yang, C., Yu, C., Dou, X., Ning, B., and Hu, L.: The global climatology of the intensity of the ionospheric sporadic E layer, *Atmos. Chem. Phys.*, 19, 4139–4151, <https://doi.org/10.5194/acp-19-4139-2019>, 2019.
- Yu, B., Scott, C. J., Xue, X., Yue, X., and Dou, X.: Derivation of global ionospheric Sporadic E critical frequency (fo Es) data from the amplitude variations in GPS/GNSS radio occultations, *Roy. Soc. Open Sci.*, 7, 200320, <https://doi.org/10.1098/rsos.200320>, 2020.
- Yu, B., Scott, C. J., Xue, X., Yue, X., and Dou, X.: Using GNSS radio occultation data to derive critical frequencies of the ionospheric sporadic E layer in real time, *GPS Solutions*, 25, 1–11, 2021a.

- Yu, B., Xue, X., Scott, C. J., Wu, J., Yue, X., Feng, W., Chi, Y., Marsh, D. R., Liu, H., Dou, X., and Plane, J. M. C.: Interhemispheric transport of metallic ions within ionospheric sporadic *E* layers by the lower thermospheric meridional circulation, *Atmos. Chem. Phys.*, 21, 4219–4230, <https://doi.org/10.5194/acp-21-4219-2021>, 2021b.
- Yu, B., Xue, X., Scott, C. J., Yue, X., and Dou, X.: An empirical model of the ionospheric sporadic E layer based on GNSS radio occultation data, *Space Weather*, 20, e2022SW003113, <https://doi.org/10.1029/2022SW003113>, 2022.
- Yu, S. and Ma, J.: Deep learning for geophysics: Current and future trends, *Rev. Geophys.*, 59, e2021RG000742, <https://doi.org/10.1029/2021RG000742>, 2021.
- Yue, X., Schreiner, W. S., Pedatella, N., Anthes, R. A., Mannucci, A. J., Straus, P. R., and Liu, J.-Y.: Space weather observations by GNSS radio occultation: From FORMOSAT-3/COSMIC to FORMOSAT-7/COSMIC-2, *Space Weather*, 12, 616–621, 2014.
- Zeng, Z. and Sokolovskiy, S.: Effect of sporadic E clouds on GPS radio occultation signals, *Geophys. Res. Lett.*, 37, L18817, <https://doi.org/10.1029/2010GL044561>, 2010.